Realization of an Extremely Anisotropic Heisenberg Magnet in Rydberg Atom Arrays

Kangheun Kim[1,*] Fan Yang,[2,*] Klaus Mølmer,[3] and Jaewook Ahn[1,†]

[1]*Department of Physics, KAIST, Daejeon 34141, Republic of Korea*
[2]*Center for Complex Quantum Systems, Department of Physics and Astronomy, Aarhus University, DK-8000 Aarhus C, Denmark*
[3]*Niels Bohr Institute, University of Copenhagen, Blegdamsvej 17, DK-2100 Copenhagen, Denmark*

Strong mutual interaction which correlates elementary excitations of quantum matter plays a key role in a range of emergent phenomena, from binding and condensation to quantum thermalization and many-body localization. Here, we employ a Rydberg quantum simulator to experimentally demonstrate strongly correlated spin transport in anisotropic Heisenberg magnets, where the magnon-magnon interaction can be tuned 2 orders of magnitude larger than the magnon hopping strength. In our approach, the motion of magnons is controlled by an induced spin-exchange interaction through far off-resonant driving, which enables coherent transport of a single Rydberg excitation across a chain of ground-state atoms. As the most prominent signature of a giant anisotropy, we show that nearby Rydberg excitations form distinct types of magnon-bound states, where a tightly bound pair exhibits frozen dynamics in a fragmented Hilbert space, while a loosely bound pair propagates and establishes correlations beyond a single lattice site. Our scheme complements studies using resonant dipole-dipole interactions between Rydberg states and opens the door to exploring quantum thermodynamics with ultrastrong interactions and kinetic constraints.

I. INTRODUCTION

Quantum simulation of spin models has established a powerful tool for unraveling exotic many-body phases and dynamics [1–7]. As a pivotal process in quantum magnetism, the quasiparticle spin excitations (magnons) can propagate through the system by coherent spin exchanges that conserve the total magnetization [8]. The inclusion of strong magnon-magnon interaction complicates the underlying spin transport, where the motion of different magnons cannot be separated [9–11]. Similar correlated transport dynamics has been observed in various quantum systems [12–18], including ultracold atoms engineered by the superexchange mechanism [13], trapped atomic ions with phonon mediated spin-spin couplings [18], and Rydberg atom arrays subjected to resonant dipole-dipole interactions [16]. These works aim to construct a spin-1/2 Heisenberg model, where the correlations can be tuned by the anisotropy of the XXZ-type Hamiltonian, defined as the strength of the magnon-magnon interaction relative to the spin-exchange rate.

One of the biggest challenges in previous experiments was to acquire a very large anisotropy, for which the strongly correlated dynamics is constrained to flip-flops that conserve not only the total magnetization but also the number of domain walls. This kinetic constraint is key to exotic nonergodic dynamics, such as Hilbert space fragmentation [19] and quantum many-body scars [20]. In this work, we demonstrate an approach that can access such an extremely anisotropic regime on a neutral-atom quantum simulator, where ground-state atoms are off-resonantly dressed to a Rydberg state to induce an effective excitation exchange [21]. As evidence of the large anisotropy, we show that the propagation of a single Rydberg excitation significantly slows down in the presence of a nearest-neighbor (NN) Rydberg excitation, due to the formation of a tightly bound state. While similar magnon-bound states have been identified in systems with short-range interactions [13] or moderate anisotropies [18], the large long-range anisotropy in our work can further support a new type of bound states with a bond length beyond the nearest neighbor.

The large anisotropy demonstrated in this work is enabled by the qubit encoding scheme we use. In a Rydberg quantum simulator, pseudo-spins can be encoded in different Rydberg manifolds, where the strong and direct

---

*These authors contributed equally to this work.
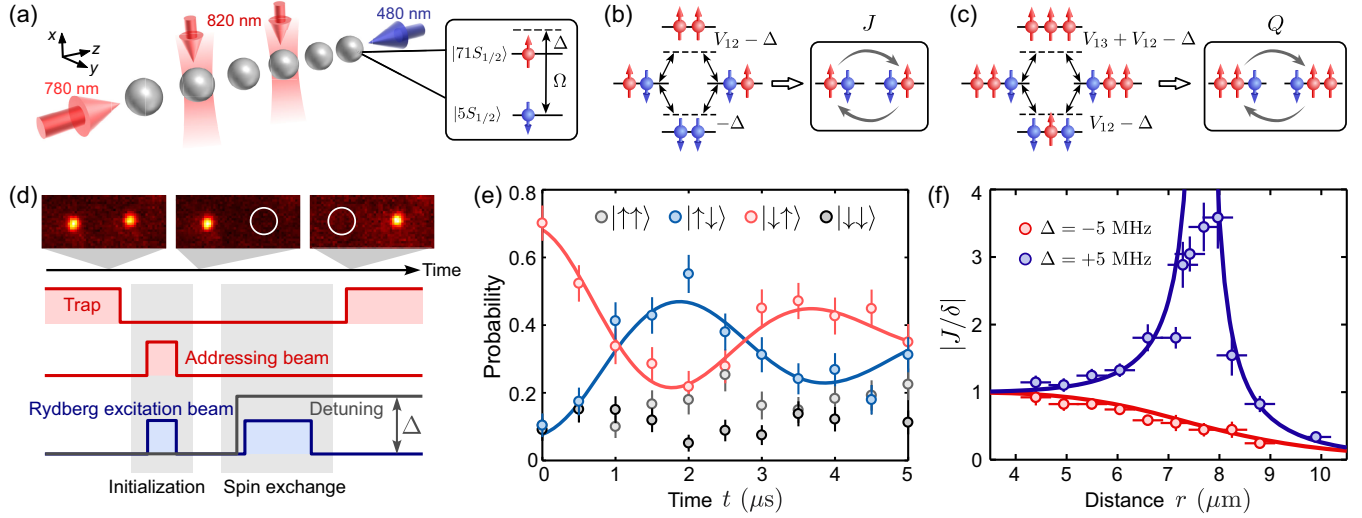†jwahn@kaist.ac.kr

FIG. 1.   Observation of spin-exchange dynamics in a Rydberg atom array. (a) In the experiment, two counterpropagating lasers of 780 and 480 nm drive a two-photon transition, which couples the ground state $|5S_{1/2}, F = 2, m_F = 2\rangle$ to the Rydberg state $|71S_{1/2}, m_J = 1/2\rangle$ via an intermediate state $|5P_{3/2}, F = 3, m_F = 3\rangle$. The trap laser of 820 nm is reused as the individual addressing beam to provide site-dependent detunings through the ac-Stark shift. Panels (b) and (c) illustrate perturbation mechanisms that induce two-body and three-body spin-exchange interactions, respectively. (d) Experimental sequence for probing the spin-exchange dynamics. For the state readout, only atoms in the ground state $|\downarrow\rangle$ are detected, while Rydberg excitations $|\uparrow\rangle$ are detected as loss (indicated by white circles). (e) Measured spin-exchange dynamics between two atoms, where the population of the states $|\uparrow\downarrow\rangle$ and $|\downarrow\uparrow\rangle$ are fitted by damped sinusoidal functions. The error bars represent the standard deviation. (f) Plot of $|J/\delta|$ as a function of the distance r. We measure the oscillating population in $|\downarrow\uparrow\rangle$ at different interatomic distances for both positive and negative detunings, and fit the data to extract the interaction strength J. The error bars represent the 2σ deviation, considering the propagation of error (see Appendix C).

dipolar interaction leads to fast coherent dynamics [16,22]. Alternatively, the spins can be represented by different ground states, which have long lifetime and can be dressed to Rydberg states to acquire weak but tunable spin-spin interactions [23–26]. For the hybrid encoding scheme using one Rydberg and one ground state, the large difference in energy scales for the spin-up and spin-down states can give rise to kinetic constraints, which behave as Rydberg blockade in the resonant driving case [1] and constrained spin exchanges in the large detuning regime studied here. The bottom-up analysis of the magnon dynamics presented in this work thus serves as an important step for understanding more complex many-body phases from the constrained dynamics [27].

II. EFFECTIVE SPIN EXCHANGE IN A RYDBERG ISING MODEL

Our experiments are carried out in a chain of ^{87}Rb atoms initially trapped in an optical tweezer array [see Fig. 1(a)]. We use a two-photon excitation scheme to couple the ground state $|\downarrow\rangle = |5S_{1/2}, F = 2, m_F = 2\rangle$ to the Rydberg state $|\uparrow\rangle = |71S_{1/2}, m_J = 1/2\rangle$, which maps the system onto a spin-1/2 chain described by a tilted Ising Hamiltonian (taking $\hbar = 1$, where $\hbar$ is the reduced Planck constant):

$$\hat{H}_{\mathrm{Ryd}} = \frac{\Omega}{2}\sum_i \hat{\sigma}_i^x - \Delta\sum_i \hat{n}_i + \frac{1}{2}\sum_{i\neq j} V_{ij}\hat{n}_i\hat{n}_j. \quad (1)$$

Here, $\hat{\sigma}_i^\alpha$ are Pauli matrices, $\hat{n}_i = |r_i\rangle\langle r_i| = (1 + \hat{\sigma}_i^z)/2$ denotes the Rydberg-state projector, and Ω and Δ are the Rabi frequency and the detuning of the two-photon transition, respectively. The interaction strength V_{ij} between Rydberg atoms at sites i and j takes the form $V_{ij} = C_6/r_{ij}^6$, where r_{ij} is the distance between the atoms and $C_6 > 0$ is the van der Waals (vdW) coefficient.

To understand the dynamics of this Rydberg Ising model, we decompose the original Hamiltonian into $\hat{H}_{\mathrm{Ryd}} = \hat{H}_0 + \hat{\Omega}_D$, where $\hat{H}_0$ is the diagonal part and $\hat{\Omega}_D = (\Omega/2)\sum_i \hat{\sigma}_i^x$ is the off-diagonal driving term that can create or annihilate a single Rydberg excitation. If we label the eigenstates of $\hat{H}_0$ according to the total Rydberg excitation number $\hat{\mathcal{N}}_R = \sum_i \hat{n}_i$, then $\hat{\Omega}_D$ only couples states where $\hat{\mathcal{N}}_R$ changes by one. As a result, the coupling usually admixes different $\hat{\mathcal{N}}_R$ subspaces. However, if the energy difference between adjacent blocks of $\hat{H}_0$ is much larger than the coupling strength Ω, these subspaces become dynamically decoupled, and only states of the same $\hat{\mathcal{N}}_R$ are coupled with each other via a perturbation

process. This perturbation effect occurs predominantly at the second order and can be described by an effective Hamiltonian $\hat{H}_{\text{eff}}$ (see Appendix A), which has a U(1) symmetry corresponding to the conserved Rydberg excitation number $\hat{\mathcal{N}}_{\text{R}}$. Figure 1(b) visualizes the perturbation process for two atoms, where states $|\uparrow\downarrow\rangle$ and $|\downarrow\uparrow\rangle$ are coupled by a spin-exchange interaction $J(\hat{\sigma}_1^+\hat{\sigma}_2^- + \hat{\sigma}_1^-\hat{\sigma}_2^+)$ between the ground state and the Rydberg state, with $\hat{\sigma}_n^\pm = (\hat{\sigma}_n^x \pm i\hat{\sigma}_n^y)/2$. Crucially, the nonvanishing interaction strength $J = \Omega^2 V_{12}/4\Delta(\Delta - V_{12})$ is enabled by unequal energy differences between adjacent $\hat{\mathcal{N}}_{\text{R}}$ sectors. These nonuniform level spacings arise from the vdW interaction and can lead to complicated magnetization-dependent spin exchanges. For example, in a three-atom chain with the central site excited to the Rydberg state [see Fig. 1(c)], the spin exchange between the first and the third atom is described by a three-body interaction term $Q(\hat{\sigma}_1^+\hat{\sigma}_3^-\hat{n}_2 + \hat{\sigma}_1^-\hat{\sigma}_3^+\hat{n}_2)$, where $Q = \Omega^2 V_{13}/4(\Delta - V_{12})(\Delta - V_{12} - V_{13})$ is the magnetization-dependent coupling strength.

To observe these virtual spin-exchange processes, it is preferable to work in the weak dressing regime $\Omega \ll |\Delta|$, which, however, results in weaker interaction strengths. Concerning this trade-off, which could be relaxed by a larger Rabi frequency, our experiments are typically performed with $|\Delta/\Omega| \in [1.5, 4]$. In this intermediate regime, we demonstrate that the U(1) symmetry is largely preserved and the deviation from the effective theory can be suppressed by a postselection measurement. Actually, we can accurately count Rydberg excitations in each experimental run by single-site resolved fluorescence imaging, which projects the spins to an exact microstate. Therefore, when exploring the dynamics of a specific $\hat{\mathcal{N}}_{\text{R}}$ subspace, events subject to processes breaking the U(1) symmetry can be discarded, while only states remaining in the given symmetry sector are retained [13]. This postselection scheme has a high success probability and shows good tolerance to imperfect state initialization.

III. QUANTUM WALK OF A SINGLE MAGNON

We first investigate the dynamics within the $\hat{\mathcal{N}}_{\text{R}} = 1$ subspace of a single Rydberg excitation (magnon). The effective Hamiltonian for this symmetry sector is a simple XY model describing coherent hopping of a single magnon: $\hat{H}_{\text{eff}} = \sum_{i<j} J_{ij}(\hat{\sigma}_i^+\hat{\sigma}_j^- + \hat{\sigma}_i^-\hat{\sigma}_j^+) + \sum_i \mu_i \hat{n}_i$, where $J_{ij} = \Omega^2 V_{ij}/4\Delta(\Delta - V_{ij})$ is the rate of the effective spin exchange, and $\mu_i = -\Delta + 2\delta + \sum_{j\neq i} J_{ij}$ is the on-site potential of the magnon with $\delta = \Omega^2/4\Delta$.

As a minimal yet nontrivial example, we begin with two sites and measure the spin-exchange process $|\downarrow\uparrow\rangle \leftrightarrow |\uparrow\downarrow\rangle$. To this end, two atoms are loaded into the tweezers and prepared in state $|\downarrow\downarrow\rangle$ via optical pumping. Then, the trap is turned off, and the first atom is addressed with a 820-nm

laser, making it off resonant with respect to the transition driven by the global Rydberg beam. The second atom is on resonant and subsequently driven to the Rydberg state by a π pulse, creating the desired initial state $|\downarrow\uparrow\rangle$. After that, the global Rydberg beam is significantly detuned to induce the effective spin exchange. The experimental sequence is shown in Fig. 1(d), and more details can be found in Ref. [28]. Figure 1(e) depicts the characteristic oscillation dynamics measured with $\Omega = 2\pi \times 1.52$ MHz, $\Delta = 2\pi \times 5$ MHz, and $r = 4.95$ μm, where r is the interatomic distance. It is clearly seen that the oscillation is approximately U(1) symmetric, as it mainly occurs in the single-excitation subspace, while states $|\downarrow\downarrow\rangle$ and $|\uparrow\uparrow\rangle$ are rarely populated. The oscillation frequency ~ 0.80 MHz drawn from the experiment agrees well with the perturbation analysis that gives $|J| \approx 0.78$ MHz. Here, the damping of the coherent spin exchange is mainly caused by uncorrelated dephasings from the intermediate-state scattering, and the scheme is intrinsically robust against correlated dephasings from the laser phase noise (see Appendix E).

We next measure the distance dependence of the interaction $J_{ij} = J(r_{ij})$ by varying the distance r between the two atoms. As shown in Fig. 1(f), the measured potential perfectly matches the theoretical prediction $J_\pm(r) = \delta/[(r/r_c)^6 \mp 1]$, where $\pm$ denotes the sign of the detuning, and $r_c = (C_6/|\Delta|)^{1/6}$ is a characteristic length. For a negative detuning ($\Delta < 0$), $J_-(r)$ is a soft-core potential that varies slowly with distance for $r < r_c$ and plateaus at δ for $r \to 0$, while it features a vdW tail $\sim 1/r^6$ for $r \gg r_c$, similar to the Rydberg-dressing induced interaction between ground-state atoms [29,30]. The potential for a positive detuning ($\Delta > 0$) has a distinct behavior: while it has the same plateau value and asymptotic scaling, $J_+(r)$ diverges at $r = r_c$. This singularity is caused by the facilitation dynamics, where the condition $V_{i,i+1} = \Delta$ makes single-magnon states resonantly coupled with the two-magnon state $|\uparrow\uparrow\rangle$, leading to a breakdown of perturbation theory and the U(1) symmetry. In the facilitation regime, it has been shown previously that a small thermal fluctuation of atomic positions can lead to a strong Anderson localization, hindering the transport of the excitation [31]. In contrast, for the U(1) symmetric regime studied in this work, the plateau of the potential makes the dynamics insensitive to the fluctuation of interatomic distance, and a magnon is expected to be highly delocalized.

To demonstrate that the magnon can exhibit a random walk behavior that is robust against atomic positional disorders, we create a larger array containing seven atoms with a spacing of 4.95 nm. In order to prepare the initial state $|\downarrow\downarrow\downarrow\uparrow\downarrow\downarrow\downarrow\rangle$, we apply the individual addressing beam to shift the detuning of the central site, followed by an adiabatic ramping of the global Rydberg beam, which only drives the atom at the center to the Rydberg state [Fig. 2(a)].
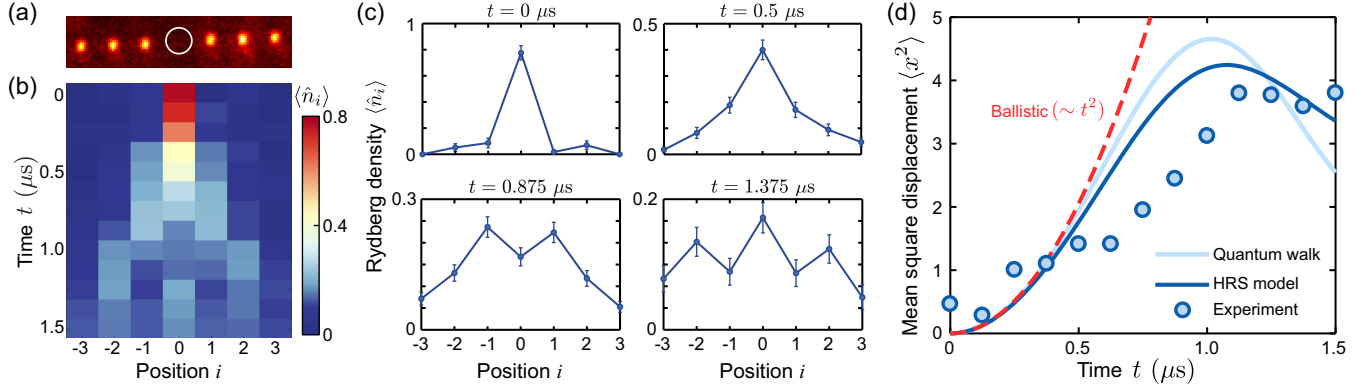
FIG. 2. Quantum random walk of a single Rydberg excitation. (a) Fluorescence image of the prepared initial state in the quench dynamics. To create the local Rydberg excitation (indicated by white circle), the atom at the central site is detuned by the addressing beam in a way that only this atom is excited by the global Rydberg beam (see Appendix B). (b) Evolution of the Rydberg density $\langle \hat{n}_i \rangle$. Here, we apply postselection and consider only data with a single Rydberg excitation. (c) Distribution of the Rydberg density $\langle \hat{n}_i \rangle$ at different times. The error bars represent the standard deviation. (d) Mean square displacement $\langle x^2 \rangle$ as a function of time. The measured data, the analytical ballistic estimations, and the calculated results are represented by the circles, the dashed lines, and the solid lines, respectively, where the dark (light) blue solid lines are calculated with (without) local dephasing. The data shown here are state-preparation-and-measurement corrected with maximum likelihood estimation (see Appendix D).

After the initialization, the addressing beam is turned off, and a red-detuned ($\Delta < 0$) Rydberg driving field is applied to induce the effective dynamics. The propagation of the initial excitation can be traced by observing the evolution of the local Rydberg density $\langle \hat{n}_i \rangle$, as shown in Fig. 2(b), where an approximate light-cone wave front can be identified. The staggered pattern of $\langle \hat{n}_i \rangle$ during the evolution is a clear evidence of the quantum interference [Fig. 2(c)], as opposed to the Gaussian distribution in a classical random walk. In the current system, the existence of uncorrelated dephasings will eventually destroy the coherence of the system and lead to a uniform steady distribution. To quantify the role of the dephasing, we extract the mean square displacement $\langle x^2 \rangle$ of the magnon [Fig. 2(d)] and find good agreement with simulations based on the Haken-Reineker-Strobl (HRS) model [32,33], which includes both coherent magnon hoppings and on-site dephasings (with a rate $\gamma = 2\pi \times 0.2$ MHz). For a larger system, the HRS model predicts that the magnon will continue to spread with no steady-state distribution, but its motion has a quantum-classical crossover: while the initial propagation for $t < 1/\gamma$ is governed by a ballistic transport ($\langle x^2 \rangle \propto t^2$), the spreading will gradually become diffusive with $\langle x^2 \rangle \propto t$. Such a scaling crossover can be identified in future experiments with increased system size.

IV. DYNAMICS OF MAGNON-BOUND STATES

Having explored the single-magnon dynamics, we proceed to the observation of correlated motions of multiple magnons. In the two-excitation subspace ($\hat{\mathcal{N}}_R = 2$), neglecting the essentially uniform on-site potential, the effective Hamiltonian now reads

$$\hat{H}_{\text{eff}} = \sum_{i<j\neq k} Q_{ijk}(\hat{\sigma}_i^+ \hat{\sigma}_j^- \hat{n}_k + \hat{n}_k \hat{\sigma}_i^- \hat{\sigma}_j^+) + \sum_{i<j} U_{ij} \hat{n}_i \hat{n}_j, \quad (2)$$

where $Q_{ijk} = (G_{ijk} + G_{jik})/2$ is the magnetization-dependent hopping strength with $G_{ijk} = \Omega^2 V_{ij}/4(\Delta - V_{ik})$ $(\Delta - V_{ik} - V_{ij})$, and $U_{ij} = V_{ij} - 4J_{ij} + \sum_{l\neq i,j}(G_{lij} - J_{li})$ denotes the density interaction between magnons. Note that the density interaction $U_{ij} \sim V_{ij}$ is mainly from the zeroth-order Hamiltonian $\hat{H}_0$, while the exchange interaction Q_{ijk} is induced by the second-order perturbation. This leads to an important characteristic that $|U_{ij}/Q_{ijk}| \sim (2\Delta/\Omega)^2 \gg 1$, which makes Eq. (2) a long-ranged, highly anisotropic Heisenberg model.

One direct consequence of this large anisotropy is the emergence of a family of magnon bound states. In an infinite spin chain, the two-magnon eigenstate $|\psi_K\rangle = \sum_{i\neq j} \psi_K(i,j)\hat{\sigma}_i^+ \hat{\sigma}_j^+ |\downarrow\downarrow \cdots \downarrow\rangle$ can be labeled by the center-of-mass momentum K, where the wave function can be factorized as $\psi_K(i,j) = e^{iKR}\phi_K(r)$ by introducing the center-of-mass position $R = (i+j)/2$ and the relative distance $r = i - j$ [34–36]. The bound state has a bounded wave function $\phi_K(\infty) \to 0$, whose energy is isolated from the scattering continuum. Therefore, systems initially in the bound state remain localized in the relative coordinate, in stark contrast to the scattering state, where individual excitations propagate freely. Figure 3(a) shows the energy spectrum and the bound-state wave function for a typical parameter $\Delta/\Omega = -3$ and $V_{i,i+1}/\Delta = -8$. The extremely large nearest-neighbor anisotropy $\xi_1 = U_{i,i+1}/Q_{i-1,i,i+1} \approx$ 684 in this case gives rise to a high-energy bound state (red curve), where magnons are tightly bounded at a relative distance $r = 1$ (nearest neighbors) for all momenta.
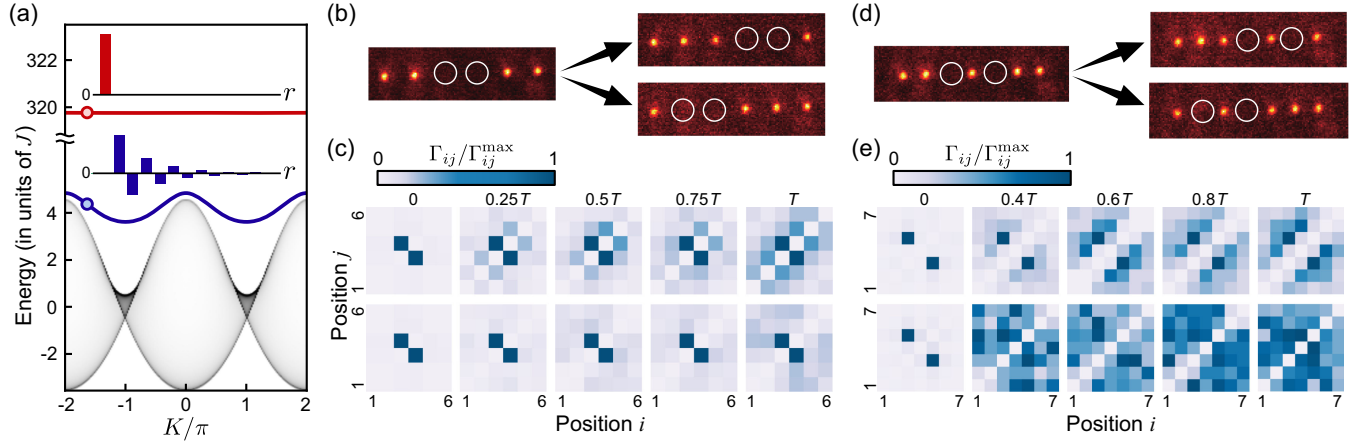
FIG. 3.   Correlated transport by magnon bound states. (a) Two-excitation spectrum for $\Delta/\Omega = -3$ and $V_{i,i+1}/\Delta = -8$, where the red (blue) curve shows the dispersion relation of the tightly (loosely) bound pair outside the continuum of scattering states (shaded area, where the gray scale indicates the density of states). The wave function $\phi_K(r)$ is illustrated (bars) for bound states of the indicated momentum (circles). (b) Correlated transport of initial Rydberg excitations (third and fourth atom, marked with white circles), mediated by a next-nearest-neighbor hopping ($3 \rightarrow 5$; or $4 \rightarrow 2$). (c) Evolution of the correlator Γ_{ij} (normalized to the maximum value $\Gamma_{ij}^{\max}$ at each given time) after preparation of nearest-neighbor pair of excitations ($T = 2.8\pi/J$). The upper panels correspond to the case with a hopping strength $Q \approx 0.13$ MHz, which reduces to $Q \approx 0.01$ MHz in the case of the lower panels (frozen dynamics). Note that the correlators for the initial state ($t = 0$) are identical for the upper and the lower panels, as they are prepared under the same experimental conditions. (d) Correlated transport of initial Rydberg excitations (third and fifth site, marked with white circles), mediated by successive nearest-neighbor hoppings ($5 \rightarrow 6$, $3 \rightarrow 4$; or $3 \rightarrow 2$, $5 \rightarrow 4$). (e) Evolution of the correlator Γ_{ij} after preparation of a next-nearest-neighbor pair of excitation ($T = 1.7\pi/J$). The upper panels are measured with a short lattice spacing for which the initial state has a large overlap ≈ 0.24 with the bound state. The lower panels are measured with a larger lattice spacing, where the initial state has a small overlap ≈ 0.09 with the bound state. The detailed experimental parameters and the exact values of $\Gamma_{ij}^{\max}$ can be found in Appendix C.

The strong density interaction also has a significant long-range effect absent in a short-range interacting system [13]: the next-nearest-neighbor (NNN) anisotropy $\xi_2 = U_{i,i+2}/Q_{i-1,i,i+2} \approx 4$ is also quite large, and can thus support a low-energy loosely bound state (blue curve), whose wave function $\phi_K(r)$ has a larger bond length $r > 1$. We will focus on these two types of bound pairs in the experiment, and expect that the same system gives rise to further varieties of bound states at larger anisotropy or in different lattice configurations.

To probe the correlated dynamics of the tightly bound Rydberg pair, we prepare an initial state $|\downarrow\downarrow\uparrow\uparrow\downarrow\downarrow\rangle$ in a six-atom chain via an adiabatic antiblockade excitation scheme, where the detuning for the center two atoms are swept across the resonant point $\Delta = V_{i,i+1}/2$. We then quench the system to a fixed detuning and measure the evolution of the two-site correlator $\Gamma_{ij} = \langle \hat{\sigma}_i^+ \hat{\sigma}_j^+ \hat{\sigma}_i^- \hat{\sigma}_j^- \rangle$. For a positive detuning $\Delta = 2\pi \times 12$ MHz, the observed correlation function propagates almost perfectly along the directions $j = i \pm 1$ [see the upper panels of Fig. 3(c)], demonstrating that two Rydberg excitations move in a correlated manner as expected [see Fig. 3(b)]. In fact, the large NN anisotropy $\xi_1 \approx -35$ in our experiment makes the total NN-Rydberg bonds $\hat{N}_{RR} = \sum_i \hat{n}_i \hat{n}_{i+1}$ another conserved charge. The tightly bound Rydberg pairs constitute the symmetry sector ($\hat{N}_R = 2, \hat{N}_{RR} = 1$), whose dynamics are governed by an NNN hopping term $Q \sum_i (\hat{\sigma}_i^+ \hat{\sigma}_{i+2}^- \hat{n}_{i+1} + \text{H.c.})$. Here, the strength $Q = Q_{i,i+2,i+1}$ corresponds to the exchange process illustrated in Fig. 1(c) and determines the propagation speed of the tightly bound pair. To further confirm this analysis, we turn the detuning to a negative value $\Delta = 2\pi \times -3.3$ MHz, with which the single-magnon hopping strength $J = J_{i,i+1}$ remains unchanged, but the magnetization-dependent hopping is significantly reduced ($Q = 0.13 \rightarrow 0.01$ MHz). Consistent with the theoretical prediction, the dynamics of the system becomes almost frozen within the timescale $T \sim 2\pi/J$ [see the lower panels of Fig. 3(c)], at which a single Rydberg excitation should already spread over the lattice. Note that the slight spreading of the correlator at late time is mainly caused by the imperfect state initialization rather than by excitation hopping. The frozen dynamics observed here is a clear signature of the Hilbert space fragmentation: while all tightly bound states $|\cdots \uparrow_i \uparrow_{i+1} \cdots\rangle$ share the local symmetry ($\hat{N}_R$ and $\hat{N}_{RR}$), they form dynamically disconnected Krylov subspaces of dimension one (frozen states). In fact, taking only NN vdW interactions into consideration (in accordance with a vanishing NNN hopping strength Q), the effective Hamiltonian can be mapped to a folded XXZ model [37–40], where spin exchanges are constrained by the conservation of $\hat{N}_{RR}$, leading to a strongly fragmented Hilbert space in the thermodynamic limit.

Unlike the tightly bound state, which has a nearly flat band in most parameter regimes (corresponding to the frozen dynamics), the loosely bound pair displays a finite bandwidth and is therefore more mobile [Fig. 3(a)]. To observe the propagation of this longer-range bound state, we prepare a seven-site chain and excite the third and the fifth atom to the Rydberg level. We first choose a small lattice spacing of 4.95 μm to achieve large anisotropies $\xi_1 = 539$ and $\xi_2 \approx 1.24$, for which the produced initial state $|\downarrow\downarrow\uparrow\downarrow\uparrow\downarrow\downarrow\rangle$ has a considerable overlap (≈ 0.24) with the loosely bound state. The upper panels of Fig. 3(e) depict the evolution of the experimentally extracted correlation function Γ_{ij}. In contrast to the tightly bound pair, whose transport is determined by an NNN hopping term, the correlated motion of the loosely bound pair is mediated by two successive NN hopping processes [Fig. 3(d)], as evident from the predominant spreading of Γ_{ij} along the directions $i = j \pm 2$. As a comparison, we then increase the interatomic distance to 8.5 μm, at which the NNN anisotropy $\xi_2 \approx -0.52$ is too small to support the long-range bound state for most values of the momenta. In this regime, the observed correlator Γ_{ij} rapidly spreads over the entire zone with no preferred propagation direction [see the lower panels of Fig. 3(e)], which suggests that the two Rydberg excitations are not bounded to each other but propagate freely [18].

To further confirm the existence of the bound state, we extract their participation ratios (BR) from the measured correlation map, where the ratios for the tightly bound state and the long-range bound state are defined as $\mathrm{BR}_1 = \sum_i \Gamma_{i,i+1}/\Gamma_{\mathrm{tot}}$ and $\mathrm{BR}_2 = \sum_i \Gamma_{i,i+2}/\Gamma_{\mathrm{tot}}$, respectively, with $\Gamma_{\mathrm{tot}} = \sum_{i<j} \Gamma_{ij}$. For the system size realized in our experiment, the reflection from the boundary can lead to a finite BR_1 and BR_2 even in the absence of magnon interactions. To estimate this finite-size effect and get a lower reference value for the participation ratio, we assume a uniform thermal distribution of the magnons with $\Gamma_{ij} = 2/L(L-1)$, where L denotes the system size. As confirmed by Fig. 4, the measured ratio is much larger than this lower bound (dashed curves) during the free-magnon relaxation time $\sim 1/J$. Here, the damping of the bound pair at late time is mainly caused by the local dephasing. It is here worth pointing out that an atomic positional disorder may slow down the propagation of bounded magnons more easily than single magnons, because it contributes a large disordered binding interaction U_{ij} (especially for the tightly bound pair). To account for the decoherence, the positional disorder, as well as other imperfections, we carry out full numerical simulations based on realistic experimental conditions and the original Rydberg Ising model (see Appendix D). This full simulation agrees very well with the experimental data and shows deviations from the perfectly coherent simulations (see Fig. 4), which suggests ways for improving the coherence of the dynamics in future studies (see Appendix E).
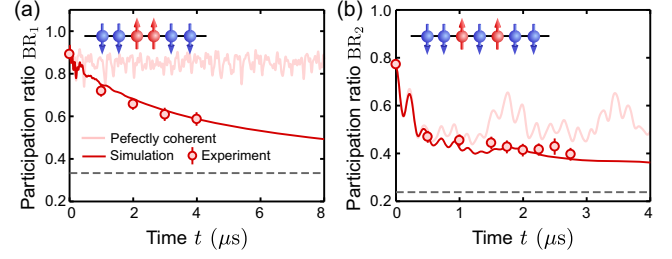

FIG. 4. Participation ratio for the tightly bound state (a) and the loosely bound state (b). The inset shows the initial spin configurations. The numerical simulation results (dark red lines) are obtained by solving a master equation, which includes the uncorrelated dephasings, as well as global laser phase noises. The simulation is averaged over 100 positional disorder realizations and takes into account imperfect state preparation and detection. The light red lines show calculations without any decoherence or disorder. The black dashed curves represent the lower bounds estimated for uniformly distributed free magnons. The error bars represent the standard deviation.

V. CONCLUSIONS AND OUTLOOK

In conclusion, we have demonstrated a new approach to constructing the Heisenberg-type spin model in a Rydberg atom array. Different from previous schemes realized by dipolar exchange interaction and Floquet engineering [16], our approach is based on far off-resonant driving in a Rydberg Ising Hamiltonian, which can offer a large and widely tunable anisotropy. In the current experiment, we focused on the single-magnon and the two-magnon sector. By improving the coherence of the system and creating more excitations in a large-scale array, the system may allow exploration of emergent Hilbert space fragmentation [39,40] and the Krylov-restricted thermalization of multiple magnons [19]. The scheme also allows dynamical engineering of spin transport, topological pumping protocols, and programmable entanglement distributions [21]. Generalizations to higher dimension could lead to richer physics. In particular, in a 2D lattice, the inclusion of a multicolor dressing field may enable application of a synthetic gauge flux [41], which can give rise to topologically protected chiral motion of the magnon-bound state and holds promise for observation of a chiral spin liquid [42].

The data reported in this paper are archived on the figshare data repository [43].

APPENDIX A: EFFECTIVE HAMILTONIAN OF THE SYSTEM

The effective U(1) symmetric model can be constructed from the Schrieffer-Wolff transformation [44]. Up to the second-order perturbation, the effective Hamiltonian is given by $\hat{H}_{\text{eff}} = \hat{H}_0 + \hat{H}_{\text{eff}}^{(2)}$ with

$$\hat{H}_{\text{eff}}^{(2)} = \hat{\mathcal{P}}\left(\frac{1}{2}[\hat{\mathcal{S}}, \hat{\Omega}_D]\right)\hat{\mathcal{P}}, \qquad (A1)$$

where $\hat{\mathcal{S}}$ is a generator satisfying $[\hat{\mathcal{S}}, \hat{H}_0] + \hat{\Omega}_D = 0$, and $\hat{\mathcal{P}}$ projects out terms that do not conserve $\hat{\mathcal{N}}_R$. Formally, the generator can be expressed as

$$\hat{\mathcal{S}} = i\frac{\Omega}{2}\sum_i \frac{\hat{\sigma}_i^y}{\Delta - \sum_{j \neq i} V_{ij}\hat{n}_j}. \qquad (A2)$$

It is difficult to get an explicit effective Hamiltonian using the above expression. Therefore, we expand $\hat{\mathcal{S}}$ in orders of the Rydberg excitation number that can influence the spin flip of a single atom at the ith site, i.e.,

$$\hat{\mathcal{S}} = (2i/\Omega)\delta\sum_i \hat{\sigma}_i^y + (2i/\Omega)\sum_{i \neq j} J_{ij}\hat{\sigma}_i^y \hat{n}_j$$
$$+ (i/\Omega)\sum_{i \neq j \neq k}(G_{ijk} - J_{ij})\hat{\sigma}_i^y \hat{n}_j \hat{n}_k + \cdots, \quad (A3)$$

where the effective coupling strengths are given by

$$\delta = \frac{\Omega^2}{4\Delta}, \qquad J_{ij} = \frac{\Omega^2 V_{ij}}{4\Delta(\Delta - V_{ij})}, \qquad (A4)$$

$$G_{ijk} = \frac{\Omega^2 V_{ij}}{4(\Delta - V_{ik})(\Delta - V_{ik} - V_{ij})}. \qquad (A5)$$

The above expansion then leads to an effective Hamiltonian $\hat{H}_{\text{eff}}^{(2)} = \hat{\mathcal{H}}_{\text{one-body}} + \hat{\mathcal{H}}_{\text{two-body}} + \hat{\mathcal{H}}_{\text{three-body}} + \cdots$, where

$$\hat{\mathcal{H}}_{\text{one-body}} = \delta\sum_i \hat{\sigma}_i^z,$$

$$\hat{\mathcal{H}}_{\text{two-body}} = \sum_{i \neq j}\frac{J_{ij}}{2}(\hat{\sigma}_i^+ \hat{\sigma}_j^- + \hat{\sigma}_i^- \hat{\sigma}_j^+ - 2\hat{\sigma}_i^z \hat{n}_j),$$

$$\hat{\mathcal{H}}_{\text{three-body}} = \sum_{i \neq j \neq k}\frac{G_{ijk} - J_{ij}}{2}(\hat{\sigma}_i^+ \hat{\sigma}_j^- + \hat{\sigma}_i^- \hat{\sigma}_j^+ - \hat{\sigma}_i^z \hat{n}_j)\hat{n}_k$$

are the one-body self-energy shift, the two-body XXZ-type Hamiltonian, and the three-body XXZ term, respectively. The Hamiltonian can be further simplified by the substitution $\hat{\sigma}_i^z = 2\hat{n}_i - 1$ in a given state sector. For the single-magnon sector ($\hat{\mathcal{N}}_R = 1$), the quadratic term $\hat{n}_i\hat{n}_j$ can be neglected, which leads to the XY model given in the main text. For the two-magnon sector ($\hat{\mathcal{N}}_R = 2$), the cubic term $\hat{n}_i\hat{n}_j\hat{n}_k$ can be discarded, and the resulting Hamiltonian can be mapped to Eq. (2). For a general multimagnon case, the dynamics is governed by a folded XXZ model exhibiting the Hilbert space fragmentation [40].

APPENDIX B: EXPERIMENTAL SETUP AND PROCEDURE

The experimental setup of our system is a Rydberg quantum simulator using a neutral atom array of ^{87}Rb atoms, similar to our previous experiments [28]. The atomic ensembles are cooled and gathered inside a magneto-optical trap, while the single atoms are trapped inside an 820-nm optical tweezer array of 1-mK depth and sub-Doppler cooled to $\sim$35 μK with polarization gradient cooling. Atoms are then optically pumped to $|\downarrow\rangle = |5S_{1/2}, F = 2, m_F = 2\rangle$. After the ground-state preparation, traps are turned off and the atoms are excited to the Rydberg state $|\uparrow\rangle = |71S_{1/2}, m_J = 1/2\rangle$ with the two Rydberg beams of 780 nm (homemade external cavity diode laser) and 480 nm (TA-SHG Pro of Toptica) with two-photon transition of intermediate detuning of $\Delta_I = 2\pi \times 660$ MHz from the intermediate state $|m\rangle = |5P_{3/2}, F = 3, m_F = 3\rangle$. Quantum operation is performed by a series of Rydberg and addressing laser pulses. After the quantum operation, atoms are trapped again by turning on the optical tweezer, and atoms in the Rydberg states are antitrapped from the tweezer. The remaining atoms are imaged with the electron-multiplied charged coupled device (EMCCD, iXon Ultra 888 of Andor) by illuminating the imaging beam. By distinguishing the fluorescence of background and trapped atom, we could determine the internal state of each individual atom.

The optical tweezer trap and the addressing beam for the state initialization use the same 820-nm laser driven from Ti: sapphire oscillator (TiC of Avesta) pumped by a 532-nm laser (Verdi G18 of Coherent). The laser beam passes an acousto-optic modulator (AOM) and is split into zeroth- and first-order beams. The first-order beam is sent to the spatial light modulator (SLM, ODPDM512 of Meadowlark optics), and the optical tweezer array of target and reservoir traps is formed and rearranged with a real-time calculation Gerchberg-Saxton weighted algorithm with graphics processing unit (Titan-X Pascal of NVIDIA). The phase for atom arrays are calculated with a 4 times larger array zero padded to the initial phase to achieve resolution less than the trap size [45]. The zeroth-order beam propagates along a different path passing an additional AOM and followed by an acousto-optic deflector (AOD, DTSXY-400-820 of AA
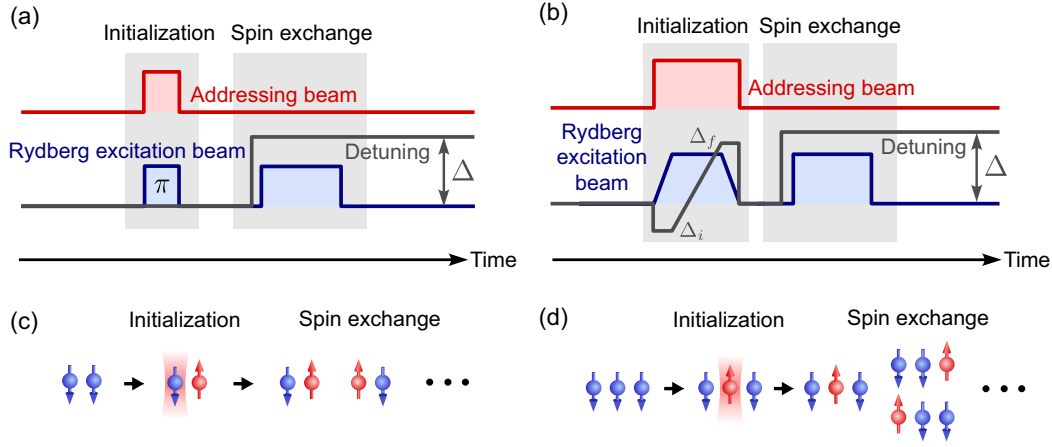
FIG. 5. Experimental sequence. (a) Sequence for the two-atom experiment illustrated in (c). (b) Sequence for the quantum walk [illustrated in (d)] and the bound-state experiments.

Opto-Electronic) which is used to address the target atom. This 820-nm addressing beam is off resonant to the $5S \rightarrow 5P$ transition, inducing an ac-Stark shift to the target-atom Rydberg transition.

The quantum operation is programmed using a delay generator (DG645 of Stanford Research Systems) and an arbitrary wave form generator (AWG, XRF Agile RF Synthesizer of Moglabs), controlling AOMs of both the addressing beams and the Rydberg beams. The sequence is depicted in Fig. 1(d) of the main text, and a more detailed sequence is given in Fig. 5. The sequence is divided into two parts: an initialization process driving the target atoms to Rydberg states and the spin-exchange process inducing the many-body quench dynamics. For the two-atom experiment, the initial state is prepared by addressing one of the atoms to make it off resonant to the Rydberg beams and applying a resonant π pulse to the other atom [see Figs. 5(a) and 5(c)]. For all other experiments, the target atoms are addressed, and the Rabi frequency Ω and the detuning Δ of the global Rydberg beams are adiabatically swept according to the following sequence: (1) $0 \rightarrow 0.1$ μs, $(0, \Delta_i) \rightarrow (\Omega_{exp}, \Delta_i)$; (2) $0.1 \rightarrow 0.9$ μs, $(\Omega_{exp}, \Delta_i) \rightarrow (\Omega_{exp}, \Delta_f)$; and (3) $0.9 \rightarrow 1$ μs, $(\Omega_{exp}, \Delta_f) \rightarrow (0, \Delta_f)$ as depicted in Fig. 5(b), where Ω_{exp} is the Rabi frequency used in the spin-exchange step. The values of these parameters are summarized in Table II. With the above initialization, the addressed target atom is adiabatically excited to the Rydberg state [see Fig. 5(d)].

APPENDIX C: EXPERIMENTAL PARAMETERS AND MEASURED VALUES

The experimental parameters are given in the tables. Table I shows the parameters and measured values for the two-atom spin-exchange dynamics, where Δ is the detuning for the spin exchange, r is the distance between the two atoms, Ω is the Rabi frequency, and J is the spin-exchange frequency fitted from each experiment, e.g., from the data

in Fig. 1(e) of the main text. The vdW interaction strength $V = C_6/r^6$ is determined by the distance r with $C_6 = 2\pi \times 1023$ GHz μm^{-6} corresponding to the Rydberg state $|71S_{1/2}, m_J = 1/2\rangle$ used in the experiment [46]. The values of Ω and J are fitted to the expression $P = a + b\cos(2\pi \times c \times t)\exp(-t/d)$ with unknowns a, b, c, d, and (post-selected) probability P of the initial state, where $\Omega/2\pi$ and $J/4\pi$ correspond to c. The horizontal error bars in Fig. 1(f) have the same value 0.3 μm for all distances, which is limited by the resolution of the image plane, where the

TABLE I. Experimental parameters, measured values, and postselected portion for the two-atom experiment.

$\Delta/2\pi$ (MHz)	r (μm)	$\Omega/2\pi$ (MHz)	$J/2\pi$ (MHz)	$2\pi J/\Omega^2$ (MHz^{-1})	$\langle P(\Pi_1)\rangle$
+5	4.4	1.52(5)	0.132(9)	0.057(5)	0.69
	4.95	1.52(5)	0.128(8)	0.055(5)	0.69
	5.5	1.52(5)	0.143(6)	0.062(5)	0.70
	6.05	1.52(5)	0.154(6)	0.066(5)	0.67
	6.6	1.52(5)	0.21(2)	0.09(1)	0.67
	7.15	1.52(5)	0.21(1)	0.09(1)	0.61
	7.29	1.52(5)	0.33(3)	0.14(2)	0.69
	7.43	1.52(5)	0.35(2)	0.15(1)	0.72
	7.7	1.52(5)	0.40(3)	0.17(2)	0.63
	7.98	1.52(5)	0.42(5)	0.18(2)	0.68
	8.25	1.52(5)	0.18(3)	0.08(2)	0.60
	8.8	1.52(5)	0.10(1)	0.041(5)	0.57
	9.9	1.52(5)	0.039(6)	0.017(3)	0.64
−5	4.4	1.86(7)	0.16(2)	0.046(6)	0.66
	4.95	1.86(7)	0.14(1)	0.041(5)	0.65
	5.5	1.52(5)	0.095(8)	0.041(4)	0.67
	6.05	1.52(5)	0.086(9)	0.037(4)	0.66
	6.6	1.52(5)	0.068(6)	0.029(3)	0.65
	7.15	1.52(5)	0.06(1)	0.027(6)	0.64
	7.7	1.86(7)	0.08(2)	0.022(5)	0.60
	8.25	1.91(9)	0.08(2)	0.022(6)	0.62
	8.8	1.91(9)	0.04(1)	0.012(3)	0.63

TABLE II. Experimental parameters and postselected portion for the quantum walk and the bound-state experiments.

Experiment	r (μm)	$\frac{\Omega_{\exp}}{2\pi}$ (MHz)	$\frac{\Delta_A}{2\pi}$ (MHz)	$\frac{\Delta_i}{2\pi}$ (MHz)	$\frac{\Delta_f}{2\pi}$ (MHz)	$\frac{\Delta_{\exp}}{2\pi}$ (MHz)	$\langle P(\Pi_2)\rangle$
Single-magnon quantum walk	4.95	2.54	−15.8	+5	+30	−5	0.40
Tightly bound state correlated transport	7	2.54	−20.3/ − 18.6	+10	+35	+12	0.32
Tightly bound state frozen motion	7	2.54	−20.3/ − 18.6	+10	+35	−3.3	0.35
Loosely bound state correlated transport	4.95	2.06	−7.4/ 5.4	+3	+15	−3	0.42
Loosely bound state free propagation	8.5	2.06	−7.4/ 5.4	+3	+15	−3	0.33

beam waist is about ~1.2 μm and the resolution is ~1.2/4 μm because of the zero padding. The vertical error bars in Fig. 1(f) and the errors for Table I indicate a 2σ confidence interval, while for all other data presented in this paper, the vertical error bars indicate a 1σ confidence interval. The estimation of the horizontal error bars in Fig. 1(f) and the errors associated with the $2\pi J/\Omega^2$ values in Table I is performed by considering the propagation of errors, expressed as $\sigma_{|J/\delta|}^2 = (\partial|J/\delta|/\partial J)^2\sigma_J^2 + (\partial|J/\delta|/\partial\Omega)^2\sigma_\Omega^2$. Table II shows the experimental parameters for the rest of the experiments. Here, $\Omega_{\exp}$ is the Rabi frequency for both spin-exchange dynamics experiment and the maximum Rabi frequency for the quantum annealing in the initial state preparation, Δ_A is the detuning applied on the target atom by the addressing beam (two values, respectively, for the left and the right atom in the two-magnon experiments), Δ_i and Δ_f are the initial and final detuning, respectively, for the detuning sweep of the state initialization, and $\Delta_{\exp}$ is the detuning for the spin-exchange quench dynamics.

In our experiments, we employ postselection to purify the measurements, where only states within a given subspace Π_n are considered ($n = 1, 2$ denotes the total Rydberg excitation). In the two-atom and the quantum walk experiment, we choose states within the single-excitation subspace (Π_1). For the two-magnon experiments, we select states within the two-excitation subspace (Π_2). The average fractions of the postselected states over the entire evolution time, denoted as $\langle P(\Pi_n)\rangle$ (success probability), are given in Tables I and II for each specific experiment. Notably, the success probability remains small and relatively stable throughout the dynamics, indicative of a largely preserved U(1) symmetry.

The maximum values $\Gamma_{ij}^{\max}$ of the measured correlator in Fig. 3 are $\{0.39, 0.13, 0.11, 0.09, 0.07\}$ for the upper panels of Fig. 3(c), $\{0.39, 0.23, 0.16, 0.16, 0.10\}$ for the lower panels of Fig. 3(c), $\{0.35, 0.10, 0.06, 0.06, 0.05\}$ for the upper panels of Fig. 3(e), and $\{0.30, 0.03, 0.03, 0.02, 0.02\}$ for the lower panels of Fig. 3(e).

APPENDIX D: EXPERIMENTAL IMPERFECTIONS AND NUMERICAL SIMULATIONS

Full numerical simulations in Fig. 4 of the main text take the experimental errors into consideration. Table III shows types of experimental imperfections and their treatment in the numerical simulations. The dominant error in the dressing scheme is the uncorrelated individual dephasing mainly due to the spontaneous decay from the intermediate state, vdW interaction fluctuation due to the finite temperature of the atom, as well as the state-measurement error. The collective dephasing mainly induced by the laser phase noise does not have a significant role on the dynamics because of the decoherence-free feature of the effective model [41]. Both individual and collective dephasings are treated with the Lindblad master equation $d\rho/dt = -i[H,\rho] + \mathcal{L}_{\mathrm{ind}}(\rho) + \mathcal{L}_{\mathrm{col}}(\rho)$ [47], where the superoperator $\mathcal{L}_{\mathrm{ind}}, \mathcal{L}_{\mathrm{col}}$ denotes the individual (on-site) and the collective phase noise, respectively. The individual dephasing rate $\gamma_{\mathrm{ind}} \approx 2\pi \times 0.2$ MHz was fitted from the three level model of $|g\rangle, |r\rangle$, and the intermediate state $|m\rangle$. The collective phase noise was fitted from the single-atom Rabi oscillation by fixing γ_{ind}, and its value is $\gamma_{\mathrm{col}} \approx 2\pi \times 0.4$ MHz. The temperature of the atomic thermal motion $T_{\mathrm{atom}} = 34.27(5)$ μK was measured using release and recapture method. With the temperature, we could calculate the

TABLE III. Experimental errors and its treatment to numerical simulations.

Error source	Treatment
Individual dephasing	$\mathcal{L}_{\mathrm{ind}} = \sum_{j=1}^N (L_j\rho L_j^\dagger - \frac{1}{2}\{L_j^\dagger L_j, \rho\})$ with $L_j = \sqrt{\gamma_{\mathrm{ind}}/2}\,\hat{n}_j$ and $\gamma_{\mathrm{ind}} \approx 2\pi \times 0.2$ MHZ
Collective dephasing	$\mathcal{L}_{\mathrm{col}} = L_0\rho L_0^\dagger - \frac{1}{2}\{L_0^\dagger L_0, \rho\}$ with $L_0 = \sqrt{\gamma_{\mathrm{col}}/2}\sum_{j=1}^N \hat{n}_j$ and $\gamma_{\mathrm{col}} \approx 2\pi \times 0.4$ MHz
Finite temperature of atoms	Monte Carlo simulation with positional fluctuation where $\sigma_{\mathrm{r}} \approx 0.1$ μm (radial) and $\sigma_{\mathrm{a}} \approx 0.3$ μm (axial)
$P(g|r)$ measurement error	$P(g|r) = 1 - \exp(-t_{\mathrm{trap}}/t_1)$ with Rydberg decay time $t_1 = 43(15)$ μs
$P(r|g)$ measurement error	$P(r|g) = P_{\mathrm{recap}}(t_{\mathrm{trap}})$ where P_{recap} is the release and recapture probability curve

position spread of atoms with a standard deviation $\sigma_i = \sqrt{k_B T/(m\omega_i^2)}$ for the trap frequency ω_i. In the simulation, the average effect of such an atomic positional disorder was evaluated with the Monte Carlo method. The radial and longitudinal position standard variations are $\sigma_r \approx 0.1$ μm and $\sigma_a \approx 0.3$ μm, respectively. The detection error was considered similar to Ref. [48], where the dominant portion of the conditional error probability $P(g|r)$ is due to the Rydberg decay and the dominant portion of $P(r|g)$ is due to a finite temperature of the atom. The former is calculated with $P(g|r) = 1 - \exp(-t_{\mathrm{trap}}/t_1)$, where t_{trap} is the time when the trap is turned off, and the Rydberg lifetime $t_1 = 43(15)$ μs is measured with an additional Ramsey experiment [49]. The latter probability $P(r|g) = P_{\mathrm{recap}}(t_{\mathrm{trap}})$ is obtained from the release and recapture probability curve.

APPENDIX E: LIMITATIONS AND POSSIBLE IMPROVEMENTS

In this appendix we discuss the limitations of the coherence in our current setup. As the Rydberg lifetime is much longer than the timescale studied, we focus here on the other four decoherence factors, including (1) collective dephasing from the laser phase noise, (2) individual dephasing from the intermediate-state scattering, (3) finite-temperature effects, and (4) the vdW force between Rydberg atoms. We also discuss how to improve the coherence of the system to satisfy the requirement for simulating complex many-body dynamics.

We first note that our scheme is intrinsically robust against collective dephasing from the laser phase noise, which can be described by including a random noise sequence $\phi(t)$ to the global Rabi frequency as $\Omega e^{i\phi(t)}$. For a complex Rabi frequency, the induced spin-exchange interaction between the ith and jth atom is $J_{ij} \propto \Omega_i \Omega_j^*$. Therefore, the global phase noise $\phi(t)$ cancels out perfectly. The robustness can also be understood from the master

equation description: If $\dot\phi(t)$ is a white noise, its influence can be described by a collective Lindblad operator $L_0 = \sqrt{\gamma_{\mathrm{col}}/2}\sum_i \hat n_i$ (see Table III), which is proportional to the total Rydberg excitation $\hat{\mathcal{N}}_R$. The fact that the effective Hamiltonian $\hat H_{\mathrm{eff}}$ conserves the total Rydberg excitation ($[\hat{\mathcal{N}}_R, \hat H_{\mathrm{eff}}] = 0$) indicates that the dynamics occurs in a decoherence-free subspace $L_0 \hat\rho = 0$. Such a robustness is numerically verified in Fig. 6(a), where the two-atom spin-exchange dynamics remains coherent for the timescale $\gg 1/\gamma_{\mathrm{col}}$.

In contrast to the collective dephasing, the individual dephasing leads to a more significant decoherence effect (see Fig. 6), which is the main limitation in our current setup. Such an individual dephasing is mainly induced by the intermediate-state scattering in our two-photon excitation scheme. For the parameters used in the experiment: $\Omega_{780} \approx 2\pi \times 80$ MHz, $\Omega_{480} \approx 2\pi \times 20$ MHZ, and an intermediate detuning $\Delta_I = 2\pi \times 660$ MHz, the dephasing rate is estimated to be $\gamma_{\mathrm{ind}} = 2\pi \times 0.2$ MHZ (see Appendix D). The typical experimental condition $r = 4.95$ μm, $\Omega = 2\pi \times 2.54$ MHz, $\Delta = 2\pi \times -5$ MHz then yields $Jt_{\mathrm{coh}} = 5$, where J is single-magnon hopping strength, and t_{coh} is the coherence time of the dynamics extracted from the numerical simulation. Two possible improvements can be made to suppress the individual dephasing: (i) using larger Rabi frequencies Ω_{780}, Ω_{480} and intermediate-state detunings Δ_I, and (ii) using single-photon transition to couple the Rydberg and the ground state. For the improvement (i), the state-of-the-art setup for the two-photon transition scheme [5,50] can achieve a large Rabi frequency $\Omega = 4.6$ MHz with an intermediate-state detuning $\Delta_I = 2\pi \times 7.8$ GHz, which requires a large laser power ~ 100 W with the flat beam of typical beam size of ~ 10 μm. The dephasing rate for this parameter is estimated to be $\gamma_{\mathrm{ind}} = 2\pi \times 0.02$ MHz, which is 10 times smaller than our current setup and can achieve a large coherence time $t_{\mathrm{coh}} \sim 20/J$. For the improvement (ii), the
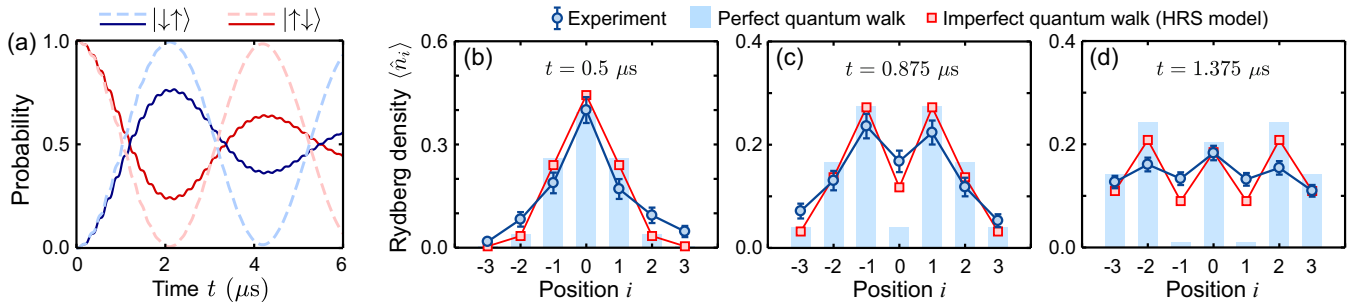

FIG. 6. (a) Numerical simulation of the two-atom spin-exchange dynamics with collective dephasing (dashed lines) and local dephasing (solid lines). The parameters correspond to the experiment performed in Fig. 1(e), and the dephasing rates are the same as in Table III. Panels (b)–(d) show the comparison between the observed and the calculated density distribution pattern during the single-magnon quantum walk dynamics. The HRS model considers coherent hoppings and local individual dephasing. The error bars represent the standard deviation.

single-photon transition scheme has been demonstrated for alkaline earth atoms such as Sr or Yb [51–53], where the transition is between a Rydberg state and a metastable intermediate state of a lifetime over one second. These improvements will make our system capable of simulating more complex many-body phenomena, such as the Krylov-restricted thermalization, which usually occurs at a time-scale $\sim 10/J$ [40].

Next we consider the effect of the finite temperature. The atomic temperature in our experiment is about 30 μK and can be further reduced by an additional cooling. Two Rydberg beams are counterpropagating, resulting in a small detuning error $k_{\text{eff}}\delta_v \sim 2\pi \times 60$ kHz from the Doppler effect, which will only cause about 0.5% of error for $\Omega = 1$ MHz. As our experiments have larger Rabi frequencies, this effect is therefore negligible. Finite temperature can also cause position fluctuation of atoms. The initial atom position fluctuation δr follows Gaussian distribution with a standard deviation $\sqrt{k_B T/m\omega_i^2}$ for each degree of freedom, where ω_i ($i = x, y, z$) are trap frequencies. For T = 30 μK and the trap frequency of $\omega_{x,y} = 2\pi \times 100$ kHz, $\omega_z = 2\pi \times 30$ kHz, the interatomic distance has an uncertainty $\delta r \sim \sqrt{2} \times 0.3$ μm, which then contributes a fluctuation of the spin-exchange rate $\delta J = [6\Delta/(V - \Delta)]J\delta r$. This effect is usually negligible for the negative detuning case, where the potential $J(r)$ varies slowly with the distance. While positional disorders have small influences on the magnon hopping, it can suppress the motion of the bound pair and the hole, and can lead to many-body localization.

The repulsion induced by the vdW force can also lead to imperfections by affecting the interatomic distance. While the single-magnon dynamics does not suffer much from this effect, dynamics for multiple Rydberg excitations can be influenced. In our current experiment, this effect does not play a significant role, because the distance between two real Rydberg excitations is quite large. For the shortest distance, 7 μm, used in the tightly bound state experiment, a classical simulation of the center-of-mass motion indicates that atoms move less than 0.04 μm during 5 μs evolution time, contributing less than 3% variations in the Rydberg interaction strength. However, this mechanical effect could be relevant if Rydberg excitations are close enough. For example, if two Rydberg atoms are separated by $r = 4.95$ μm, they will be pushed away from each other by 1 μm in 10 μs, resulting in 3 times smaller Rydberg interaction than at the initial position. To prevent this effect, one needs to trap both Rydberg and ground-state atoms, which can be achieved by using ponderomotive bottle beam trapping [54] or using alkaline earth atoms which overcomes the ponderomotive force by the core potential [52]. To further suppress the decoherence caused by motional excitation (phonon), one may implement a sympathetic cooling scheme as proposed in a recent theoretical work [55].

[1] H. Bernien, S. Schwartz, A. Keesling, H. Levine, A. Omran, H. Pichler, S. Choi, A. S. Zibrov, M. Endres, M. Greiner, V. Vuletić, and M. D. Lukin, *Probing many-body dynamics on a 51-atom quantum simulator*, Nature (London) **551**, 579 (2017).

[2] J. Zhang, G. Pagano, P. W. Hess, A. Kyprianidis, P. Becker, H. Kaplan, A. V. Gorshkov, Z.-X. Gong, and C. Monroe, *Observation of a many-body dynamical phase transition with a 53-qubit quantum simulator*, Nature (London) **551**, 601 (2017).

[3] C. Gross and I. Bloch, *Quantum simulations with ultracold atoms in optical lattices*, Science **357**, 995 (2017).

[4] H. Kim, Y. J. Park, K. Kim, H. S. Sim, and J. Ahn, *Detailed balance of thermalization dynamics in Rydberg-atom quantum simulators*, Phys. Rev. Lett. **120**, 180502 (2018).

[5] S. Ebadi, T. T. Wang, H. Levine, A. Keesling, G. Semeghini, A. Omran, D. Bluvstein, R. Samajdar, H. Pichler, W. W. Ho, S. Choi, S. Sachdev, M. Greiner, V. Vuletić, and M. D. Lukin, *Quantum phases of matter on a 256-atom programmable quantum simulator*, Nature (London) **595**, 227 (2021).

[6] P. Scholl, M. Schuler, H. J. Williams, A. A. Eberharter, D. Barredo, K.-N. Schymik, V. Lienhard, L.-P. Henry, T. C. Lang, T. Lahaye, A. M. Läuchli, and A. Browaeys, *Quantum simulation of 2D antiferromagnets with hundreds of Rydberg atoms*, Nature (London) **595**, 233 (2021).

[7] C. Chen, G. Bornet, M. Bintz, G. Emperauger, L. Leclerc, V. S. Liu, P. Scholl, D. Barredo, J. Hauschild, S. Chatterjee, M. Schuler, A. M. Läuchli, M. P. Zaletel, T. Lahaye, N. Y. Yao, and A. Browaeys, *Continuous symmetry breaking in a two-dimensional Rydberg array*, Nature (London) **616**, 691 (2023).

[8] A. Auerbach, *Interacting Electrons and Quantum Magnetism* (Springer Science & Business Media, New York, 1998).

[9] H. Bethe, *Zur theorie der metalle*, Z. Phys. **71**, 205 (1931).

[10] M. Wortis, *Bound states of two spin waves in the Heisenberg ferromagnet*, Phys. Rev. **132**, 85 (1963).

[11] M. Ganahl, E. Rabel, F. H. L. Essler, and H. G. Evertz, *Observation of complex bound states in the spin-1/2 Heisenberg XXZ chain using local quantum quenches*, Phys. Rev. Lett. **108**, 077206 (2012).

[12] K. Winkler, G. Thalhammer, F. Lang, R. Grimm, J. Hecker Denschlag, A. Daley, A. Kantian, H. Büchler, and P. Zoller, *Repulsively bound atom pairs in an optical lattice*, Nature (London) **441**, 853 (2006).

[13] T. Fukuhara, P. Schauß, M. Endres, S. Hild, M. Cheneau, I. Bloch, and C. Gross, *Microscopic observation of magnon bound states and their dynamics*, Nature (London) **502**, 76 (2013).

[14] P. M. Preiss, R. Ma, M. E. Tai, A. Lukin, M. Rispoli, P. Zupancic, Y. Lahini, R. Islam, and M. Greiner, *Strongly correlated quantum walks in optical lattices*, Science **347**, 1229 (2015).

[15] Z. Yan, Y.-R. Zhang, M. Gong, Y. Wu, Y. Zheng, S. Li, C. Wang, F. Liang, J. Lin, Y. Xu *et al.*, *Strongly correlated quantum walks with a 12-qubit superconducting processor*, Science **364**, 753 (2019).

[16] P. Scholl, H. J. Williams, G. Bornet, F. Wallner, D. Barredo, L. Henriet, A. Signoles, C. Hainaut, T. Franz, S. Geier, A. Tebben, A. Salzinger, G. Zürn, T. Lahaye, M. Weidemüller,

and A. Browaeys, *Microwave engineering of programmable XXZ Hamiltonians in arrays of Rydberg atoms*, PRX Quantum **3,** 020303 (2022).

[17] A. Morvan, T. Andersen, X. Mi, C. Neill, A. Petukhov, K. Kechedzhi, D. Abanin, A. Michailidis, R. Acharya, F. Arute *et al.*, *Formation of robust bound states of interacting microwave photons*, Nature (London) **612,** 240 (2022).

[18] F. Kranzl, S. Birnkammer, M. K. Joshi, A. Bastianello, R. Blatt, M. Knap, and C. F. Roos, *Observation of magnon bound states in the long-range, anisotropic Heisenberg model*, Phys. Rev. X **13,** 031017 (2023).

[19] N. Regnault, S. Moudgalya, and B. A. Bernevig, *Quantum many-body scars and Hilbert space fragmentation: A review of exact results*, Rep. Prog. Phys. **85,** 086501 (2022).

[20] C. J. Turner, A. A. Michailidis, D. A. Abanin, M. Serbyn, and Z. Papić, *Weak ergodicity breaking from quantum many-body scars*, Nat. Phys. **14,** 745 (2018).

[21] F. Yang, S. Yang, and L. You, *Quantum transport of Rydberg excitons with synthetic spin-exchange interactions*, Phys. Rev. Lett. **123,** 063001 (2019).

[22] Y. Chew, T. Tomita, T. P. Mahesh, S. Sugawa, S. de Léséleuc, and K. Ohmori, *Ultrafast energy exchange between two single Rydberg atoms on a nanosecond timescale*, Nat. Photonics **16,** 724 (2022).

[23] Y.-Y. Jau, A. Hankin, T. Keating, I. H. Deutsch, and G. Biedermann, *Entangling atomic spins with a Rydberg-dressed spin-flip blockade*, Nat. Phys. **12,** 71 (2016).

[24] J. Zeiher, R. Van Bijnen, P. Schauß, S. Hild, J.-y. Choi, T. Pohl, I. Bloch, and C. Gross, *Many-body interferometry of a Rydberg-dressed spin lattice*, Nat. Phys. **12,** 1095 (2016).

[25] N. Schine, A. W. Young, W. J. Eckner, M. J. Martin, and A. M. Kaufman, *Long-lived Bell states in an array of optical clock qubits*, Nat. Phys. **18,** 1067 (2022).

[26] L.-M. Steinert, P. Osterholz, R. Eberhard, L. Festa, N. Lorenz, Z. Chen, A. Trautmann, and C. Gross, *Spatially tunable spin interactions in neutral atom arrays*, Phys. Rev. Lett. **130,** 243001 (2023).

[27] G. Semeghini, H. Levine, A. Keesling, S. Ebadi, T. T. Wang, D. Bluvstein, R. Verresen, H. Pichler, M. Kalinowski, R. Samajdar *et al.*, *Probing topological spin liquids on a programmable quantum simulator*, Science **374,** 1242 (2021).

[28] K. Kim and J. Ahn, *Quantum tomography of Rydberg atom graphs by configurable ancillas*, PRX Quantum **4,** 020316 (2023).

[29] J. E. Johnson and S. L. Rolston, *Interactions between Rydberg-dressed atoms*, Phys. Rev. A **82,** 033412 (2010).

[30] N. Henkel, R. Nath, and T. Pohl, Three-dimensional roton excitations and supersolid formation in Rydberg-excited Bose-Einstein condensates, Phys. Rev. Lett. **104,** 195302 (2010).

[31] M. Marcuzzi, J. Minář, D. Barredo, S. de Léséleuc, H. Labuhn, T. Lahaye, A. Browaeys, E. Levi, and I. Lesanovsky, *Facilitation dynamics and localization phenomena in Rydberg lattice gases with position disorder*, Phys. Rev. Lett. **118,** 063606 (2017).

[32] H. Haken and P. Reineker, *The coupled coherent and incoherent motion of excitons and its influence on the line shape of optical absorption*, Z. Phys. **249,** 253 (1972).

[33] H. Haken and G. Strobl, *An exactly solvable model for coherent and incoherent exciton motion*, Z. Phys. **262,** 135 (1973).

[34] R. Piil and K. Mølmer, *Tunneling couplings in discrete lattices, single-particle band structure, and eigenstates of interacting atom pairs*, Phys. Rev. A **76,** 023607 (2007).

[35] M. Valiente and D. Petrosyan, *Scattering resonances and two-particle bound states of the extended Hubbard model*, J. Phys. B **42,** 121001 (2009).

[36] F. Letscher and D. Petrosyan, *Mobile bound states of Rydberg excitations in a lattice*, Phys. Rev. A **97,** 043415 (2018).

[37] G. De Tomasi, D. Hetterich, P. Sala, and F. Pollmann, *Dynamics of strongly interacting systems: From Fock-space fragmentation to many-body localization*, Phys. Rev. B **100,** 214313 (2019).

[38] Z.-C. Yang, F. Liu, A. V. Gorshkov, and T. Iadecola, *Hilbert-space fragmentation from strict confinement*, Phys. Rev. Lett. **124,** 207602 (2020).

[39] A. Yoshinaga, H. Hakoshima, T. Imoto, Y. Matsuzaki, and R. Hamazaki, *Emergence of Hilbert space fragmentation in Ising models with a weak transverse field*, Phys. Rev. Lett. **129,** 090602 (2022).

[40] F. Yang, H. Yarloo, H.-C. Zhang, K. Mølmer, and A. E. B. Nielsen, *Probing Hilbert space fragmentation with strongly interacting Rydberg atoms* (to be published).

[41] X. Wu, F. Yang, S. Yang, K. Mølmer, T. Pohl, M. K. Tey, and L. You, *Manipulating synthetic gauge fluxes via multicolor dressing of Rydberg-atom arrays*, Phys. Rev. Res. **4,** L032046 (2022).

[42] S. Weber, R. Bai, N. Makki, J. Mögerle, T. Lahaye, A. Browaeys, M. Daghofer, N. Lang, and H. P. Büchler, *Experimentally accessible scheme for a fractional Chern insulator in Rydberg atoms*, PRX Quantum **3,** 030302 (2022).

[43] K. Kim, F. Yang, K. Mølmer, and J. Ahn, *Realization of an extremely anisotropic Heisenberg magnet in Rydberg atom arrays*, figshare (2023), 10.6084/m9.figshare.24903246.

[44] S. Bravyi, D. P. DiVincenzo, and D. Loss, *Schrieffer-Wolff transformation for quantum many-body systems*, Ann. Phys. (Amsterdam) **326,** 2793 (2011).

[45] H. Kim, M. Kim, W. Lee, and J. Ahn, *Gerchberg-Saxton algorithm for fast and efficient atom rearrangement in optical tweezer traps*, Opt. Express **27,** 2184 (2019).

[46] S. Weber, C. Tresp, H. Menke, A. Urvoy, O. Firstenberg, H. P. Büchler, and S. Hofferberth, *Calculation of Rydberg interaction potentials*, J. Phys. B **50,** 133001 (2017).

[47] W. Lee, M. Kim, H. Jo, Y. Song, and J. Ahn, *Coherent and dissipative dynamics of entangled few-body systems of Rydberg atoms*, Phys. Rev. A **99,** 043404 (2019).

[48] S. de Léséleuc, D. Barredo, V. Lienhard, A. Browaeys, and T. Lahaye, *Analysis of imperfections in the coherent optical excitation of single atoms to Rydberg states*, Phys. Rev. A **97,** 053803 (2018).

[49] H. Levine, A. Keesling, A. Omran, H. Bernien, S. Schwartz, A. S. Zibrov, M. Endres, M. Greiner, V. Vuletić, and M. D. Lukin, *High-fidelity control and entanglement of Rydberg-atom qubits*, Phys. Rev. Lett. **121,** 123603 (2018).

[50] S. J. Evered, D. Bluvstein, M. Kalinowski, S. Ebadi, T. Manovitz, H. Zhou, S. H. Li, A. A. Geim, T. T. Wang,

N. Maskara, H. Levine, G. Semeghini, M. Greiner, V. Vuletić, and M. D. Lukin, *High-fidelity parallel entangling gates on a neutral-atom quantum computer*, Nature (London) **622**, 268 (2023).

[51] I. S. Madjarov, J. P. Covey, A. L. Shaw, J. Choi, A. Kale, A. Cooper, H. Pichler, V. Schkolnik, J. R. Williams, and M. Endres, *High-fidelity entanglement and detection of alkaline-earth Rydberg atoms*, Nat. Phys. **16**, 857 (2020).

[52] J. T. Wilson, S. Saskin, Y. Meng, S. Ma, R. Dilip, A. P. Burgers, and J. D. Thompson, *Trapping alkaline earth Rydberg atoms optical tweezer arrays*, Phys. Rev. Lett. **128**, 033201 (2022).

[53] A. P. Burgers, *Frontiers in quantum science with* Yb *atom arrays*, in *Quantum Computing, Communication, and Simulation III*, edited by Philip R. Hemmer and Alan L. Migdall, SPIE Proceedings Vol. 12446 (SPIE-International Society for Optical Engineering, Bellingham, WA, 2023), pp. 11–16.

[54] D. Barredo, V. Lienhard, P. Scholl, S. de Léséleuc, T. Boulier, A. Browaeys, and T. Lahaye, *Three-dimensional trapping of individual Rydberg atoms in ponderomotive bottle beam traps*, Phys. Rev. Lett. **124**, 023201 (2020).

[55] R. Belyansky, J. T. Young, P. Bienias, Z. Eldredge, A. M. Kaufman, P. Zoller, and A. V. Gorshkov, *Nondestructive cooling of an atomic quantum register via state-insensitive Rydberg interactions*, Phys. Rev. Lett. **123**, 213603 (2019).